Measurement of the local diattenuation and retardance of thin polymer films using near-field polarimetry

Lori S. Goldner,[1] Michael J. Fasolka,[2] Scott N. Goldie[1,3]

National Institute of Standards and Technology Gaithersburg, MD 20899
[1]Optical Technology Division, Physics Laboratory
[2]Polymers Division, Materials Science and Engineering Laboratory.
[3]Current Address: Shire Laboratories, Rockville, MD 20850

Near-field scanning optical microscopy and Fourier analysis polarimetry are combined to obtain quantitative maps of the local retardance, (resulting from strain or crystalline birefringence), fast axis orientation, diattenuation and diattenuating axis orientation in nanostructured polymer thin films. Lateral resolution of 50 nm with retardance sensitivity as small as 1 mrad has been demonstrated in images of isotactic PS crystallites and diblock copolymer morphologies.

Many techniques are available to study strain and order in bulk polymers, but observing local structure in thin films is complicated by the difficulty of sample preparation, small contrast requiring high sensitivity, and a need for high spatial resolution. Ellipsometry and polarimetry provide high sensitivity but lack spatial resolution necessary for characterizing sub-micron structures. Transmission electron microscopy offers high spatial resolution but requires difficult sample preparations. Aperture-based near-field scanning optical microscopy (*1, 2*) (NSOM) provides a means to measure and view structures as

small as 20 nm in size, but most often gives only qualitative images. Here we demonstrate a quantitative extension of NSOM that permits high sensitivity measurements of local optical properties.

Simple static near-field polarimetry (NFP), where a specific polarization state of light is used to excite the sample and another polarization state is detected, has been discussed by many authors (*3-6*) in many different contexts, including investigations of small metal structures (*3, 6*), magnetic films (*3, 7, 8*), lipid films (*9*), J-aggregates (*10*), conjugated polymers (*11-14*) and liquid crystal (LC) droplet structure, dynamics (*15*) and birefringence (*15, 16*). The introduction of polarization modulation techniques to NSOM (*4*) increased both the quality and the information content of polarimetric images. For example, Ade *et al.* (*17*) used a modulating analyzer to improve on static polarimetry measurements; by modulating the analyzer one can obtain both parallel- and crossed-polarizer images simultaneously. Polarization modulation (PM) of the excitation light was used in conjunction with NSOM by Higgins *et al.* to measure the orientation of mesoscopic crystals (*18*), and by the group of H. Heinzelmann to study magnetic materials and liquid crystals (*19-21*). Correcting for tip diattenuation (*22*), Tan *et al.* (*23*) and Wei *et al.* (*24*) used the same technique to study diattenuation of conjugated polymers. Other PM schemes in NSOM can be found (*25-30*). Our scheme most closely resembles that of J.W.P Hsu, whose group studied the local retardance of semiconductors (*31*).

Here we describe our implementation and application of NFP to thin polymer films. The analysis required for measurements of local retardance and diattenuation, including the orientation of corresponding optical axes, is discussed, and the importance of accurately accounting for the diattenuation and residual birefringence of the near-field probe is stressed. Systems studied include (1) ultrahigh molecular weight block copolymers (*32-34*) which microphase separate (*35*) to form domains patterned on a ≈100 nm length scale and (2) polymer crystallites grown in thin films of isotactic polystyrene.

Polarimetric near-field scanning optical microscope

Excellent reviews of NSOM have been written by Pohl (*36*), Betzig (*37*), and more recently Dunn (*38*). A schematic of our NSOM polarimeter is shown in Fig. 1 and described in more detail in Ref. (*39*). A polarizer prepares linearly polarized light at 0°. The polarization generator consists of a Hinds Instruments photoeleastic modulator (PEM) tuned to a nominal modulation frequency $\omega = 50$ kHz, and a modulation axis oriented at -45° followed by a quarter wave retarder (QWR) oriented with fast axis at -90°. A fiber coupler and near-field fiber-probe are positioned before the sample, and a microscope
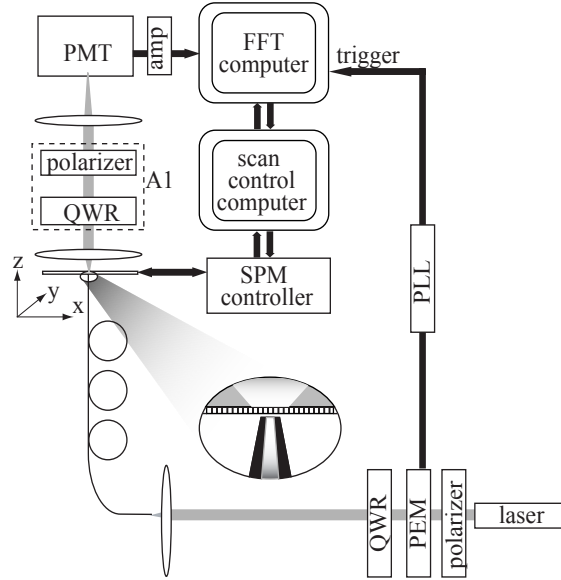
Figure 1. Schematic illustration of the NSOM polarimeter. A linear polarizer is followed by a PEM with modulation axis at -45° and quarter wave retarder (QWR) oriented with fast axis at -90°. A circular analyzer, A1, (QWR with fast axis at 0° and linear polarizer at -45°) follows the sample for birefringence measurements.. Fiber paddles are shown as loops. Inset illustrates the NSOM aperture probe.

objective (numerical aperture 0.85) is inserted just after the sample to collect the transmitted light. We use aluminum-coated pulled single-mode fiber probes (*40*) with aperture sizes from 50 nm to 180 nm. The aperture is held 5 nm to 10 nm from the sample using a shear-force feedback mechanism (*41*) that employs a small piezo-electric tube to sense tip motion. The sample is scanned using a piezo-driven flexure stage. To ensure a 1 MHz bandwidth (single pole), the detector, a photomultiplier tube (PMT), is run at high gain and the current amplifier at low gain (20 μA/V) and high bandwidth. A fast digital I/O board is used to acquire optical data; topographic data is acquired using a scanning probe microscope (SPM) control system (RHK SPM 1000 version 8).

At each pixel in an image, 8192 intensity data points (or more) spaced by $\pi/4\omega \cong 2.5$ μs are acquired. A phase-locked loop locks the sampling frequency to a multiple of the resonant PEM frequency, so the 1ω and 2ω components of a fast Fourier transform (FFT) of the intensity can be easily recovered. That is, the Fourier component representing the positive PEM frequency is

commensurate with the 1024th point in our transform, and twice that frequency is commensurate with the 2048th point. As we will see below, these intensity modulations are the result of diattenuation or birefringence or both in the sample. An FFT of the intensity vs. time signal then yields the amplitude of the dc component and the amplitude and phase (or real and imaginary parts) of the 1ω and 2ω components, which are recorded. The digital I/O board and the SPM software are located on separate computers; hardware handshaking implemented between the two computers permits simultaneous acquisition of all optical and topographic data. Each point in the image takes 20 ms (for 8192 intensity points) to 80 ms (for 32k intensity points) to acquire so a 128 by 128 image takes a minimum of about 6 minutes to acquire; actual acquisition time (including deadtime during the handshake) was between 20 mins. and 2 hours.

Probe diattenuation and retardance must be considered when implementing polarization modulation in a near-field microscope. All near-field probes have diattenuation arising from asymmetries in the probe aperture or tip coating. An improperly coupled fiber will have additional diattenuation from reflections at the cleaved end (*31*), although careful cleaving and coupling can eliminate this. Fiber probes also have linear or circular retardance from strain birefringence or geometrical considerations in the fiber tail. The linear retardance of a non-diattenuating fiber can be nulled using a commercially available fiber polarization controller, sometimes called "fiber paddles" (e.g. Thorlabs Inc., FPC030). However, in the presence of a diattenuating tip, we show below that the fiber retardance cannot be nulled, only minimized; the residual birefringence must be accounted for. Circular birefringence of the fiber contributes an overall rotation of the incoming polarization, so absolute orientations cannot be determined a priori. In this work, *the diattenuating and fast axis orientations are always measured relative to an unknown but fixed axis (31).*

Polarization modulation polarimetry with Fourier analysis

In polarimetry, the change in polarization of light as it passes through a sample is measured and used to ascertain the properties of a material. A typical polarimeter places a sample between a polarization state generator and a polarization state analyzer. The polarimetric properties of a homogeneous, stationary material can be described by 8 parameters: a global phase change (corresponding to the average index-of-refraction of a material), a global absorption or transmission, two eigenpolarizations (polarizations for which light propagates through the materials with no polarization state change) specified by 4 parameters (each has an angle and a ellipticity), and the relative phase change and relative absorption (or relative transmittance) for eigenpolarized light (ratio of the eigenvalues). We concentrate here on 5 parameters that may be described

by (1) the overall absorption or transmittance, (2) the relative absorption (dichroism) or transmittance (diattenuation) of the two eigenpolarizations, (3) linear birefringence (or more generally, the linear retardance), and (4) the orientations of the fast and (5) dichroic or diattenuating axes. The use of a polarization modulation technique (*42, 43*), described next, permits us to measure these 5 parameters in two passes over the sample (two different analyzer configurations).

For a linear diattenuator with transmittances given by *q* and *r* (*q>r),* we define diattenuation as:

$$D = \frac{q-r}{q+r} , \tag{1}$$

where q is the transmittance of light polarized parallel to the *diattenuating axis*, and r is the transmittance of light polarized perpendicular to this axis. Note, light polarized along the diattenuating axis has the higher transmittance. Likewise, for a linear retarder we define the retardance as a difference between phase shifts along the ordinary and extraordinary axis of retarder;

$$\theta = 2\pi \cdot (n_o - n') \cdot t / \lambda . \tag{2}$$

Here λ is the wavelength of light, *t* is the thickness of the sample, n_o is the ordinary index of refraction, and *n′* is the effective extraordinary index of the film. For a uniaxial crystal with the symmetry axis tilted at angle α from the propagation direction, *n′* is given by:

$$1/n' = \sqrt{\cos^2 \alpha / n_o + \sin^2 \alpha / n_e} , \tag{3}$$

where n_e is the extraordinary index (for light polarized along the symmetry axis). For a non-crystalline polymer we have

$$\theta = 2\pi \cdot \Delta n \cdot t \cdot f / \lambda , \tag{4}$$

where *f* is a factor characterizing the orientation of the chains; *f* = 1 for a perfectly aligned chain and *f* = 0 for random orientation. The intrinsic birefringence of the polymer, Δn, and the birefringence of the crystalline form (n_o-n_e) will generally be quite different.

Our instrument (described above, Fig. 1) is based on a polarization modulation polarimetry scheme described in Refs. (*42, 43*). The combination of linear polarizer, PEM and QWR results in light at the input to the fiber that is

linearly polarized, with a polarization direction that is modulated at frequency $\omega/2\pi$ Hz through an angle d given by the modulation amplitude of the PEM. This light passes through the tip and sample to be collected by the PMT. A circular analyzer, A1 in Fig. 1 (QWR oriented with its fast axis at 0º followed by a linear polarizer at -45º), may be inserted after the sample for measurements of retardance. If a linear retardance is present, the light will have a circular component whose amplitude changes with the input polarization direction. Accordingly, the detected signal after A1 will have harmonics of $\omega/2\pi$ Hz. To measure the linear diattenuation, A1 is removed and the intensity of the transmitted light at the detector is measured directly. An overall transmitted intensity that changes with incident linear polarization direction is an indicator of sample diattenuation and the magnitude and direction of the diattenuation can be extracted from the periodicity and amplitude of the signal. In general, the signal at the detector can be written

$$I(t) = I_0 + I_1 \sin(\omega t) + I_2 \cos(2\omega t) + ... \tag{5}$$

where I_0, I_1, and I_2 will be determined with and without A1 in place to determine the 5 parameters of interest to us here: the overall transmission, the diattenuation, the direction of the diattenuating axis, the linear retardance, and the direction of the "fast" or low index axis.

The parameters I_0, I_1, and I_2 are extracted from the FFT [$F(v)$] of the intensity signal at the PMT;

$$F(0) = I_0 \tag{6}$$

$$\mathrm{Im}\big(F(\omega)\big) = -I_1 / 2 \tag{7}$$

$$\mathrm{Re}\big(F(2\omega)\big) = I_2 / 2 \tag{8}$$

With no sample and only the NSOM probe in place, we find the following relationships between the amplitudes I_0, I_1, and I_2 of Eqs. (5)–(8) and the retardance and diattenuation of the probe (*39*). With A1 removed:

$$R_{1\omega}^t \equiv I_1 / I_0 = 2D_t J_1(d)[\sin(2\varphi_b^t)\cos(2\varphi_d^t - 2\varphi_b^t) + \cos(\theta_t)\cos(2\varphi_b^t)\sin(2\varphi_d^t - 2\varphi_b^t)] \tag{9}$$

$$R_{2\omega}^t \equiv I_2 / I_0 = 2D_t J_2(d)[\cos(2\varphi_b^t)\cos(2\varphi_d^t - 2\varphi_b^t) - \cos(\theta_t)\sin(2\varphi_b^t)\sin(2\varphi_d^t - 2\varphi_b^t)] \tag{10}$$

Here $D_t = (u-v)/(u+v)$ is the diattenuation of the NSOM probe or tip and φ_d^t is the alignment angle of the diattenuating axis; θ_t is the retardance of the probe and φ_b^t is the alignment of the fast axis. The amplitude of the PEM phase modulation is given by d and the PEM frequency is $\omega/2\pi$ Hz. The amplitude $d = 2.405$ is chosen so that the zeroth order Bessel function $J_0(d) = 0$, which gives $J_1(d) \cong 0.519$ and $J_2(d) \cong 0.432$. Notice that both terms are proportional to D_t with factors that depend on both the orientation of the fast and diattenuating axes *and* the cosine of the probe retardance. As we demonstrate below, if the diattenuation of the tip is not too large, the retardance of the probe can be made small (but not zero), using the fiber-paddles and fiber-nulling procedure described by McDaniel *et al.* (*31*). To this end, we expand these equations for small θ_t (< 0.1) so that $\cos(\theta_t) \cong 1$. The error involved in this approximation will be of order θ_t^2, which for our probes will always be less than 0.01. In this case we can approximate Eqs. (9) and (10) by :

$$R_{1\omega}^t \cong 2D_t J_1(d)\sin(2\varphi_d^t) \tag{11}$$

$$R_{2\omega}^t \cong 2D_t J_2(d)\cos(2\varphi_d^t), \tag{12}$$

which we can use to determine the diattenuation of the tip.

For the case where A1 is in, we can show that the intensity at the PMT has Fourier components:

$$B_{1\omega}^t \equiv I_1 / I_0 = R_{1\omega}^t + 2J_1(d)\left(2\frac{\sqrt{uv}}{u+v}\sin(\theta_t)\cos(2\varphi_b^t)\right) \tag{13}$$

$$B_{2\omega}^t \equiv I_2 / I_0 = R_{2\omega}^t - 2J_2(d)\left(2\frac{\sqrt{uv}}{u+v}\sin(\theta_t)\sin(2\varphi_b^t)\right) \tag{14}$$

Here, it is apparent that most of dependence on diattenuation can be accounted for (without approximation) by a simple subtraction of the diattenuation measurement from the retardance measurement. This pattern repeats itself when measuring sample retardance in the presence of tip and sample diattenuation.

If the tip diattenuation is small, we can apply a further approximation to simplify the expressions above. For small diattenuation such that

$$\frac{\sqrt{uv}}{u+v} = \frac{1}{2}\sqrt{1 - D_t^2} = \frac{1}{2}\left(1 - \frac{1}{2}D_t^2 + ...\right) \cong 1/2 ,$$ (15)

we see that Eqs. (13) and (14) can be written as:

$$B_{1\omega}^t \cong R_{1\omega}^t + 2J_1(d)\sin(\theta_t)\cos(2\varphi_b^t)$$ (16)

$$B_{2\omega}^t \cong R_{2\omega}^t - 2J_2(d)\sin(\theta_t)\sin(2\varphi_b^t) .$$ (17)

To minimize fiber probe birefringence and permit the use of the approximation that gives Eqs. (11) and (12), we adjust the fiber paddles shown to zero $B_{1\omega}^t$ and $B_{2\omega}^t$ within the noise limit ("nulling"). If $D_t = 0$, this would guarantee $\theta_t = 0$. D_t is never zero but for most tips it is below 0.1. Therefore nulling gives $R_{1\omega}^t \cong -2J_1(d)\left(\sin(\theta_t)\cos(2\varphi_b^t)\right)$ and $R_{2\omega}^t \cong 2J_2(d)\left(\sin(\theta_t)\sin(2\varphi_b^t)\right)$. Using Eqs. (11) and (12) and recalling that $d = 2.405$, we find that that $|\sin(\theta_t)| \approx D_t$. Eqs. (11) and (12) can therefore be used after nulling if $D_t < 0.1$.

To measure the retardance and diattenuation of a sample, we assume: (1) that samples are both diattenuating and birefringent, but that the retardance and diattenuation are small – a reasonable expectation for thin polymer films and (2) that $D_t < 0.1$, so that θ_t can be kept small as discussed above. In this case, the full expression for the ratios of the Fourier components of the measured intensity are, for A1 removed (diattenuation measurement) (*39*):

$$R_{1\omega}^s \cong 2J_1(d)\left[D_t \sin(2\varphi_d^t) + D_s \sin(2\varphi_d^s)\right];$$ (18)

$$R_{2\omega}^s \cong 2J_2(d)\left[D_t \cos(2\varphi_d^t) + D_s \cos(2\varphi_d^s)\right].$$ (19)

Here D_s is the sample diattenuation and φ_d^t is the orientation of the diattenuating axis. We use the same approximations as above for both tip and sample diattenuation and retardance, which gives Eqs. (18) and (19) correct to second order in $\theta_s, \theta_t, D_t, D_s$, and their products. Similarly, the ratios of the Fourier components for a retardance measurement (A1 in) are as follows:

$$B_{1\omega}^s \cong R_{1\omega}^s + 2J_1(d)\left[\sin(\theta_t)\cos(2\varphi_b^t) + \sin(\theta_s)\cos(2\varphi_b^s)\right]; \tag{20}$$

$$B_{2\omega}^s \cong R_{2\omega}^s - 2J_2(d)\left[\sin(\theta_t)\sin(2\varphi_b^t) + \sin(\theta_s)\sin(2\varphi_b^s)\right]. \tag{21}$$

Where θ_s is the sample retardance and φ_b^s the orientation of the sample fast axis. Eqs. (18) and (19) (and the tip properties) are used to arrive at the sample diattenuation. To determine the sample retardance, we first measure the diattenuation of the sample and then subtract $R_{1\omega}^s$ and $R_{2\omega}^s$ directly from the result of our retardance measurement, as suggested by Eqs. (20) and (21). Note that the tip diattenuation need not be explicitly accounted for in the retardance measurement if this procedure is followed. A more complete discussion of this analysis can be found in Ref. (*39*).

NFP of Photonic Block Copolymer Morphology

A study of block copolymer (BC) lamellar morphology by NFP (*32*) is summarized here. Microphase separation in BCs, driven by the immiscibility of the end-connected constituent polymer chains or *blocks*, produces a variety of domain motifs (lamellae, double-gyroid, hexagonal-packed cylinders and BCC spheres) with a related set of 1-, 2- and 3-dimensional band structures (*44-46*), tunable through the BC composition (*35, 47*). A BC's molecular mass (M_r) governs the microphase domain periodicity (L_0), typically limited to a range of 10 nm - 100 nm. However, recent synthetic efforts have produced ultra-high molecular mass BCs with L_0 of 150 nm - 300 nm, enabling M_r-tailored photonic band gaps in the visible (*33, 48, 49*). This morphological flexibility is complimented by an extensive set of techniques geared to perfect/control the order of BC structures and furnish them with added functionality (*50*). These strategies can be harnessed to enhance the optical performance of BC materials and devices based upon them. The optical activity of single microphase domains and defect structures may dictate device function; the advance of photonic BC systems requires a technique to characterize optical properties at the mesoscale.

Polystyrene-b-polyisoprene (PS-b-PI) block copolymer ($M_r = 1.4 \times 10^6$) used here is nearly volume-symmetric in composition (PS/PI = 480K/560K), and exhibits the lamellar microdomain motif with $L_0 \approx 240$ nm. Bulk specimens were processed by roll casting, which helps order and align the domains (*51*).

Thin (100 nm) sections were sliced from the bulk using cryo-ultramicrotomy and deposited onto glass coverslips. Subsequent exposure to OsO_4 vapor (2 hours) preferentially crosslinks the PI domains, making them less mechanically compliant (more amenable to shear-force feedback), and enhancing the optical contrast between PS and PI. Single lamellar domains and defects are resolved in transmission (Fig. 2b). The PI domains ($n = 1.52$, stained) appear darker, while PS domains ($n = 1.59$) appear lighter, as verified through the topography image (Fig. 2d) and plot in Fig. 2, which demonstrate that darker domains are also lower in height, due to PI contraction during OsO_4 crosslinking.

Fig. 2a maps the diattenuation of a BC specimen (analyzed using Eqs. 18 and 19) with simultaneously acquired topography and transmission micrographs. The optical images (Fig. 2a-c), and in particular the diattenuation image (Fig. 2a), provide excellent morphological detail. Comparison of the diattenuation (Fig. 2a) and transmission (Fig. 2b) along the white line (Fig. 2, right) show that the higher-transmitting PS domains appear most diattenuating (3 % to 5 %), the absorbing PI domains appear less diattenuating (2 % to 4 %), and that D_s is minimized near the domain interface. An explanation for this pattern of D_s is suggested by the Bethe-Bowkamp model (BB) (*52, 53*), which approximates the field at an NSOM aperture. In BB, the field pattern at the tip is elongated along the polarization axis. This anisotropic field pattern centered over an absorbing PI domain, transmits less/more when polarized parallel/perpendicular to the domain, producing apparent diattenuation (*39*). For the less absorbing PS domains, the opposite is true. Indeed, φ_d^s (Fig. 2c) alternates between domains with a difference $\approx 90°$. The diattenuation here is therefore not intrinsic to the sample but an artifact of the tip/sample interaction.

Fig. 3 focuses on a symmetric tilt boundary where the lamella bend through two "kinks" along an "N"-shaped track. The diattenuation images (c,e) are used (with probe data) to correct the birefringence images (d,f), via Eqs. (20) and (21). As in Fig. 2, the D_s image (Fig. 3c) illuminates the domain and interface morphology across the defect. The retardance (θ_s) is mapped in Fig. 3d. The standard uncertainty is ± 10 mrad (*39*). Contrast here is governed by Eq. (4) which relates θ_s to the sample thickness (t), the intrinsic birefringence (Δn), the illumination wavelength ($\lambda = 488$ nm) and the degree of chain orientation (f) (*54*). Inter-domain contrast is therefore based upon the difference in Δn between PS ($\Delta n = 0.195$ for atactic PS) (*54*) and PI ($\Delta n = 0.13$) (*55*), and f, which reflects the net average elongation of chains perpendicular to the interface exhibited by ordered BC systems. Thus, PS domains appear lighter (larger θ_s), while PI domains appear darker, as verified by comparing Fig. 3d with Fig. 3b. Contrast across the defect is dictated by f, and t. In principle θ_s is proportional to the local stress (through f), but variations in the through-plane lamellar orientation, *i.e.* "projection effects" due to arbitrary sectioning of the specimen, may also affect θ_s. Indeed, as expected with projection effects, θ_s

often seems inversely related to the apparent L_0 observed in this image. In-plane lamellar orientation is illuminated in Fig. 3f, which maps the relative φ_b^s. Due to chain elongation, the low-n axis lies perpendicular to the domain interface; φ_b^s reflects this. As the lamellae bend though the symmetric tilt boundary, φ_b^s increases and decreases accordingly. Discontinuities in the φ_b^s image are due to phase wrapping.

NFP of polymer crystallites

The characteristic spherulite crystallization pattern of bulk polymers has been studied for many years, but other morphologies, especially those that occur in otherwise amorphous thin films undergoing "cold" crystallization, present measurement difficulties (*56-62*) and so have been less studied. Traditional methods most often lack the spatial resolution and/or sensitivity required to examine 1) chain conformations near the growth front, 2) amorphous layers posited to exist between lamellae, and 3) the orientation of folded chains within these crystallites. NFP is well suited to the study of thin films and can be used to elucidate structure and the character of the strain field in these non-equilibrium crystallization patterns.

Polymers crystallize by forming folded layers (lamellae). In isotactic polystyrene (iPS), studied here and in Refs. (*63, 64*), these lamellae organize on a larger scale into hexagonal crystals with 6-fold symmetry around the chain (c) axis. Polystyrene is therefore a uniaxial crystal with a fast c axis. In a sufficiently thin film (thickness less than the radius of gyration of the polymer, R_g), crystallites one lamellar thickness will form in a variety of hexagonally symmetric and branching morphologies, generally with the c axis perpendicular to the substrate. At the top and bottom surfaces of each lamella, the polymer chains loop back on themselves and a thin amorphous layer should be expected and has been reported (*65*). A boundary depleted of polymer (depletion boundary) forms around the growing crystallite as polymer from the less-dense amorphous region is pulled into the crystallite (*65*). In thicker films spherulites can form and the lamella stack and the chain axis can tilt or twist (*66*). An amorphous layer above the folded lamellae and depletion region around the growing crystal pattern should still be present.

Two separate morphologies, an early-growth spherulite and a dendritic, "compact seaweed" morphology (*67-69*), are shown here in Figs. 4-6. Samples were prepared as discussed in Refs. (*63, 64*). Film thickness was approximately 85 nm for the spherulites and 15 nm for the dendrites.

Fig. 4a shows shear-force images of typical crystallites with seaweed morphology (*67-69*) taken with a sharp NSOM probe (*40*). The thickness of

these films is less than the radius of gyration for the iPS ($R_g = 22$ nm), so the crystallites are a single lamella thick. Fig. 4b shows an AFM image of a typical spherulite. In both cases, depletion regions, with low topography, are seen around the edges of the pattern and a thick nucleation site is visible in the center.

NFP images of a seaweed pattern are shown in Fig. 5. The topography image (Fig. 5b) is lower resolution that those of Fig. 1; good NSOM tips are flat with a diameter of approximately 400 nm (40), giving poor topographic images. Fig. 5a shows a birefringent structure in an otherwise amorphous ($\theta = 0$) film. Birefringence is highest at the center of pattern (the nucleation site), around the edges (in the depletion boundary, where 6 mrad $< \theta <$ 10 mrad) and near the growth tips. The noise floor (standard deviation) is 0.6 mrad for this image. The fast axis orientation is shown with lines overlaid on the retardance and topography images in Figs. 5c and d. The fast axis lines are drawn with length proportional to θ, and have been omitted where the $\theta < 2.0$ mrad. An overall shift of 0.45 rad has been applied to the fast axis orientation to bring polymer in the depletion region into radial alignment.

In this image the main source of birefringence is most likely strain in the amorphous layers. In similar crystallites, Taguchi *et al.* have found that the c axis is always within 6° of normal to the surface (70-72), which would result in $\theta < 1$ mrad from Eq. 2 and 3 [for iPS, $<n> = 1.6$ (54) and n_o-$n_e = 0.28$ ($73, 74$); the intrinsic birefringence $\Delta n = 0.167$ ($54, 73, 75$)]. A stressed amorphous layer only 5 nm thick has maximum $\theta = 10$ mrad (for $f = 1$, from Eq. 4); a 15 nm thick strained amorphous film has maximum $\theta = 32$ mrad. The stress in amorphous regions or layers can account for most if not all of the retardance in Fig. 5.

In Figure 6 we show NFP images of a spherulite. A second crystallite is adjacent on the right side. If a -1.12 rad shift is applied globally to the fast axis orientation data, we again see a depletion region consistent with radial strain. The retardance in this region is 20 mrad $< \theta <$ 30 mrad. Here the uncertainty on the retardance (one standard deviation) is 5 mrad. Healing of the fast axis direction from radial to circumferential as we move in radially towards the center of the spherulite is evident, except at 5 angles at which the radial alignment persists to the center. For two other (isolated) spherulites, there were 6 such incursions (63). For amorphous iPS with $f = 1$, the maximum retardance for an 84 nm thick film is 183 mrad (Eq. 4), roughly twice the measured maximum. The retardance measured in Fig. 6 is greater than could possibly be due to strain in a thin amorphous layer but less than is possible for iPS perfectly aligned with c axis parallel to the substrate. It seems likely that θ reflects a combination of strain in the amorphous regions and tilt of the chain axis in the crystalline form.

Summary and Conclusions

In many respects, NFP is a natural extension of classical micro-polarimetry that has been used with great success to understand stress and crystallization in thicker polymer materials (*66*). We expect other innovations first pioneered using far-field techniques might be adapted for near-field use and correspondingly greater resolution. The adaptation of Fourier polarimetry, using polarization modulation and a real-time FFT, already has several advantages over static techniques or the use of lock-in amplifiers. First, it is a more flexible system, permitting extension of the Fourier analysis to more frequency components, and therefore more optical properties, without adding electronics. Second, this setup permits the use of a single input channel to collect all the polarimetric data. This concern is particularly relevant to the integration of polarimetry with NSOM, where each input channel must be synchronized with the position of a scanning stage and the number of input channels is often limited. This design makes it possible to easily incorporate more generalized polarimetry, such as that described in Refs. (*76, 77*) since an arbitrary number of Fourier components can be monitored without need for further input channels.

We have shown how NFP can be used to map out the linear diattentuation and birefringence of thin polymer samples, and we have briefly discussed the origins of these optical properties. Quantitative modeling that takes into account both the physical properties of the films and artifacts due to tip-sample interactions remain to be developed.

References

1. E. Betzig, A. Lewis, A. Harootunian, et al. *Biophys. J.* **1986**, *49*, 269-279.
2. D. W. Pohl, W. Denk and M. Lanz. *Appl. Phys. Lett.* **1984**, *44*, 651-653.

3. E. Betzig, J. K. Trautman, J. S. Weiner, et al. *Appl. Optics* **1992**, *31*, 4563-4568.
4. M. Vaeziravani and R. Toledocrow. *Appl. Phys. Lett.* **1993**, *63*, 138-140.
5. R. Toledocrow, J. K. Rogers, F. Seiferth, et al. *Ultramicroscopy* **1995**, *57*, 293-297.
6. G. A. Valaskovic, M. Holton and G. H. Morrison. *J. Microsc.-Oxf.* **1995**, *179*, 29-54.
7. T. J. Silva and S. Schultz. *Rev. Sci. Instrum.* **1996**, *67*, 715-725.
8. E. Betzig, J. K. Trautman, R. Wolfe, et al. Appl. Phys. Lett. 1992, 61, 142-144.
9. A. Jalocha and N. F. van Hulst. *J. Opt. Soc. Am. B-Opt. Phys.* **1995**, *12*, 1577-1580.
10. D. A. Higgins, P. J. Reid and P. F. Barbara. *J. Phys. Chem.* **1996**, *100*, 1174-1180.
11. J. A. DeAro, K. D. Weston, S. K. Buratto, et al. *Chem. Phys. Lett.* **1997**, *277*, 532-538.
12. J. A. Teetsov and D. A. Vanden Bout. *J. Am. Chem. Soc.* **2001**, *123*, 3605-3606.
13. J. Teetsov and D. A. Vanden Bout. *Macromol. Symp.* **2001**, *167*, 153-166.
14. J. Teetsov and D. A. Vanden Bout. *Langmuir* **2002**, *18*, 897-903.
15. D. A. Higgins, X. M. Liao, J. E. Hall, et al. *J. Phys. Chem. B* **2001**, *105*, 5874-5882.
16. E. Mei and D. A. Higgins. *J. Chem. Phys.* **2000**, *112*, 7839-7847.
17. H. Ade, R. ToledoCrow, M. VaezIravani, et al. *Langmuir* **1996**, *12*, 231-234.
18. D. A. Higgins, D. A. VandenBout, J. Kerimo, et al. *J. Phys. Chem.* **1996**, *100*, 13794-13803.
19. T. Lacoste, T. Huser, R. Prioli, et al. *Ultramicroscopy* **1998**, *71*, 333-340.
20. T. Lacoste, T. Huser and H. Heinzelmann. *Z. Phys. B-Condens. Mat.* **1997**, *104*, 183-184.
21. T. Huser, T. Lacoste, H. Heinzelmann, et al. *J. Chem. Phys.* **1998**, *108*, 7876-7880.
22. P. K. Wei and W. S. Fann. *J. Microsc.-Oxf.* **2001**, *202*, 148-153.
23. C. H. Tan, A. R. Inigo, J. H. Hsu, et al. *J. Phys. Chem. Solids* **2001**, *62*, 1643-1654.
24. P. K. Wei, Y. F. Lin, W. Fann, et al. *Phys. Rev. B* **2001**, *6304*, 045417.
25. T. J. Silva, S. Schultz and D. Weller. *Appl. Phys. Lett.* **1994**, *65*, 658-660.
26. V. Kottler, N. Essaidi, N. Ronarch, et al. *J. Magn. Magn. Mater.* **1997**, *165*, 398-400.
27. P. Fumagalli, A. Rosenberger, G. Eggers, et al. *Appl. Phys. Lett.* **1998**, *72*, 2803-2805.

28. O. Bergossi, H. Wioland, S. Hudlet, et al. *Jpn. J. Appl. Phys. Part 2 - Lett.* **1999**, *38*, L655-L658.
29. T. Roder, L. Paelke, N. Held, et al. *Rev. Sci. Instrum.* **2000**, *71*, 2759-2764.
30. L. Ramoino, M. Labardi, N. Maghelli, et al. *Rev. Sci. Instrum.* **2002**, *73*, 2051-2056.
31. E. B. McDaniel, S. C. McClain and J. W. P. Hsu. *Appl. Optics* **1998**, *37*, 84-92.
32. M. J. Fasolka, L. S. Goldner, J. Hwang, et al. *Phys. Rev. Lett.* **2003**, *90,* 016107.
33. A. Urbas, Y. Fink and E. L. Thomas. *Macromolecules* **1999**, *32*, 4748-4750.
34. A. C. Edrington, A. M. Urbas, P. DeRege, et al. *Adv. Mater.* **2001**, *13*, 421-425.
35. F. S. Bates and G. H. Fredrickson. *Annu. Rev. Phys. Chem.* **1990**, *41*, 525.
36. D. W. Pohl. *Advances in optical and electron microscopy* **1991**, *12*, 243.
37. E. Betzig and J. K. Trautman. *Science* **1992**, *257*, 189-195.
38. R. C. Dunn. *Chem. Rev.* **1999**, *99*, 2891-+.
39. L. S. Goldner, M. J. Fasolka, S. Nougier, et al. *Appl. Optics* **2003**, *42*, 3864-3881.
40. E. Betzig, J. K. Trautman, T. D. Harris, et al. *Science* **1991**, *251*, 1468-1470.
41. E. Betzig, P. L. Finn and J. S. Weiner. *Appl. Phys. Lett.* **1992**, *60*, 2484-2486.
42. P. L. Frattini and G. G. Fuller. *J. Colloid Interface Sci.* **1984**, *100*, 506-518.
43. S. J. Johnson, P. L. Frattini and G. G. Fuller. *J. Colloid Interface Sci.* **1985**, *104*, 440-455.
44. Y. Fink, A. M. Urbas, M. G. Bawendi, et al. *J. Lightwave Technol.* **1999**, *17*, 1963-1969.
45. M. Maldovan, A. M. Urbas, M. Yufa, et al. *Phys. Rev. B* **2002**, *65*, 165123.
46. A. M. Urbas and E. L. Thomas. Bicontinuous Cubic Photonic Crystal in a Block Copolymer System, 2002
47. E. L. Thomas and R. L. Lescanec. *Philos. Trans. R. Soc. Lond. Ser. A-Math. Phys. Eng. Sci.* **1994**, *348*, 149-166.
48. A. Urbas, R. Sharp, Y. Fink, et al. *Adv. Mater.* **2000**, *12*, 812-814.
49. A. C. Edrington, A. M. Urbas, P. DeRege, et al. *Adv. Mater.* **2001**, *13*, 421.
50. M. J. Fasolka and A. M. Mayes. *Annu. Rev. Mat. Res.* **2001**, *31*, 323.
51. R. J. Albalak and E. L. Thomas. *J. Polym. Sci. Pt. B-Polym. Phys.* **1994**, *32*, 341-350.
52. H. A. Bethe. *Phys. Rev.* **1944**, *66*, 163.
53. C. J. Bowkamp. *Philips Res. Rep.* **1950**, *5*, 321.
54. *Polymer Handbook*; 4th ed.; J. Brandrup, E. H. Immergut and E. A. Grulke, Eds.; Johh Wiley & Sons, Inc.: New York, 1999

55. M. Hashiyama, R. G. Gaylord and R. S. Stein. *Makromol. Chem. Suppl.* **1975**, *1*, 579.
56. K. Izumi, G. Ping, M. Hashimoto, et al. Crystal Growth of Polymers in Thin Films. In *Advances in Understanding of Crystal Growth Mechanisms*; T. Nishinaga, K. Nishioka, J. Harada, A. Sasaki and H. Takei, Eds.; Elsevier Science: Amsterdam, 1997; pp 337-348.
57. R. L. Jones, S. K. Kumar, D. L. Ho, et al. *Macromolecules* **2001**, *34*, 559-567.
58. O. Mellbring, S. K. Oiseth, A. Krozer, et al. *Macromolecules* **2001**, *34*, 7496.
59. G. Reiter. *Europhys. Lett.* **1993**, *23*, 579-584.
60. G. Reiter and J.-U. Sommer. *J. Chem. Phys.* **2000**, *112*, 4376-4383.
61. Y. Sakai, M. Imai, K. Kaji, et al. *J. Cryst. Growth* **1999**, *203*, 244.
62. S. Sawamura, H. Miyaji, K. Izumi, et al. *J. Phys. Soc. Japan* **1998**, *67*, 3338-3344.
63. L. S. Goldner, S. N. Goldie, M. J. Fasolka, et al. *in press, Appl. Phys. Lett.* **2004**.
64. S. N. Goldie, M. J. Fasolka, L. S. Goldner, et al. *Polym. Mater. Sci. Eng.* **2003**, *88*, 145.
65. K. Izumi, P. Gan, A. Toda, et al. *Japanese Journal of Applied Physics* **1994**, *33*, L 1628 - L 1630.
66. B. Wunderlich *Macromolecular Physics*; Academic Press: New York, 1973
67. E. Brener, H. Muller-Krumbhaar, D. Tempkin, et al. *Physica A* **1998**, *249*, 73-81.
68. V. Ferreiro, J. F. Douglas, J. Warren, et al. *Phys. Rev. E* **2002**, *65*.
69. V. Ferreiro, J. F. Douglas, J. A. Warren, et al. *Phys. Rev. E* **2002**, *65*.
70. K. Taguchi, H. Miyaji, K. Izumi, et al. *Polymer* **2001**, *42*, 7443-7447.
71. K. Taguchi, H. Miyaji, K. Izumi, et al. *J. Macromol. Sci.-Phys.* **2002**, *B41*, 1033-1042.
72. K. Taguchi, Y. Miyamoto, H. Miyaji, et al. *Macromolecules* **2003**, *36*, 5208-5213.
73. E. F. Gurnee. *J. Appl. Phys.* **1954**, *25*, 1232-1240.
74. R. S. Stein. *J. Appl. Phys.* **1961**, *32*, 1280-1286.
75. V. N. Tsevtkov. *Journal of Polymer Science* **1962**, *57*, 727-741.
76. G. E. Jellison and F. A. Modine. *Appl. Optics* **1997**, *36*, 8184-8189.
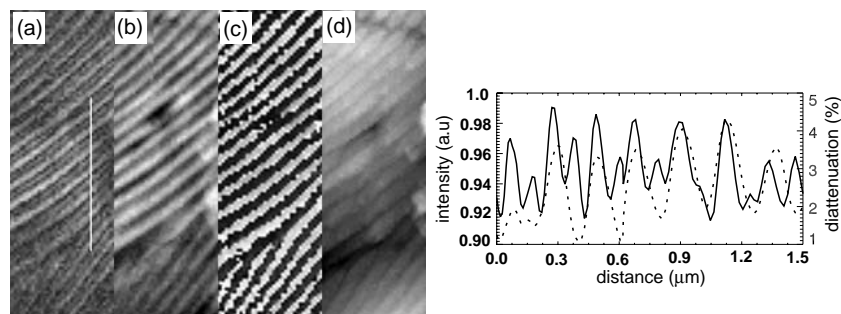77. G. E. Jellison and F. A. Modine. *Appl. Optics* **1997**, *36*, 8190-8198.

*Figure 2. Left: NFP data from a BC specimen. (a) diattenuation [0 % -5 %],
(b) transmission (normalized intensity) [0.6-1.0], (c) orientation of the
diattenuating axis orientation [0°-180°], (d) topography [0 nm - 25 nm]. Right:
diattenuation (solid line) and transmitted intensity (dotted line) along the white
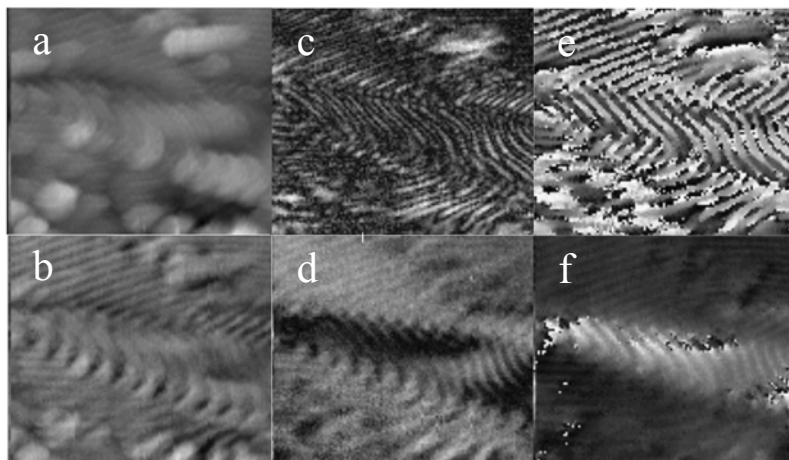line shown in (a).*

*Figure 3. NFP images of BC sample showing a symmetric tilt boundary. (a)
topography [0 nm - 25 nm], (b) transmission [0.8 – 1.0], (c) diattenuation [0 %
- 9 %], (d) retardance [0 mrad – 122 mrad], (e) relative angle of diattenuating
axis [0°-180°], (f) relative angle of fast axis [0°-180°]. Scan size is 3.0 μm by
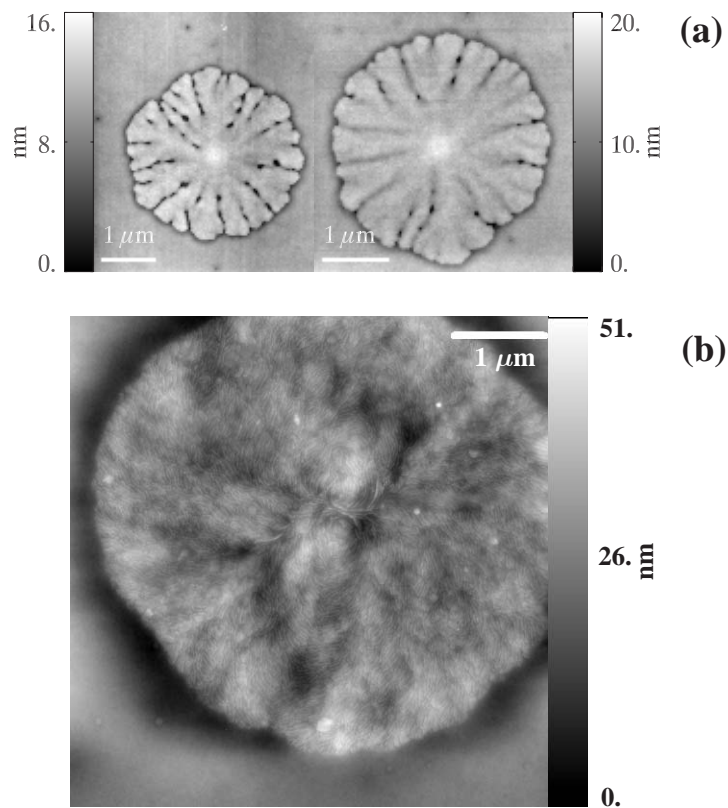3.6 μm*

Figure 4. Topographic images of polymer crystallites studied here. Top: dendritic crystallites with compact seaweed morphology, images acquired using shear-force microscopy and an NSOM tip. Bottom: early-growth stage spherulite. Image acquired using AFM.
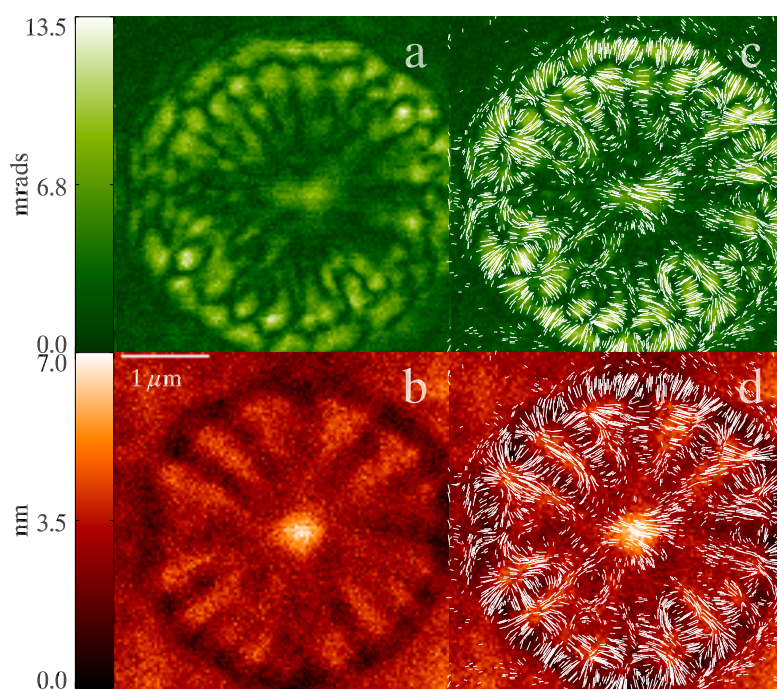
Figure 5 (Left). NFP images of compact seaweed morphology dendrite. (a) retardance, (b) topography, (c) retardance with overlaid fast axis orientation marks, (d) topography with overlaid fast axis orientation marks. Fast axis alignment shown for θ > 2.0 mrad.
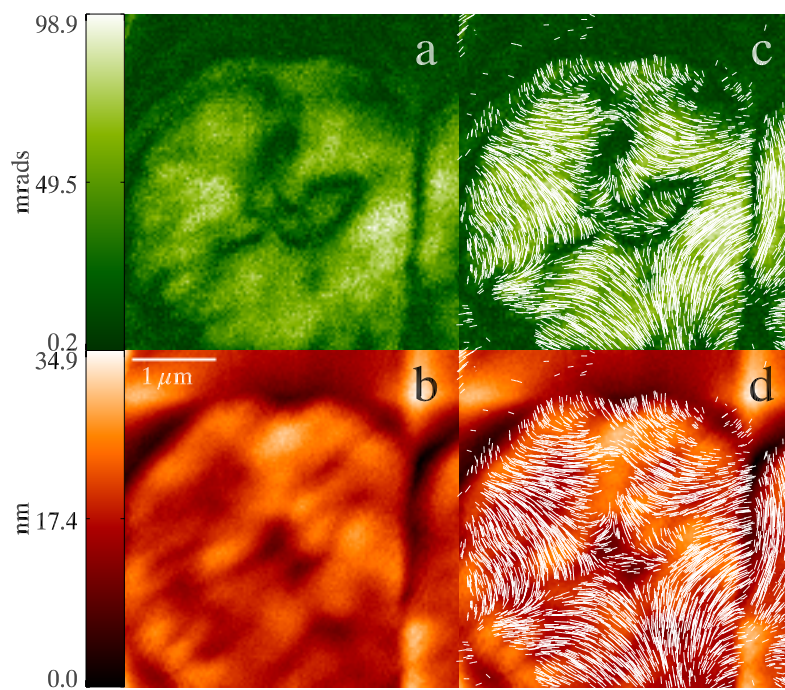
Figure 6. NFP images of an early-growth spherulite. (a) retardance, (b) topography, (c) retardance with overlaid fast axis orientation marks, (d) topography with overlaid fast axis orientation marks. Fast axis alignment shown for $\theta > 20$ mrad.